

Magnetic domain-wall velocity oscillations in permalloy nanowires

Jusang Yang, Corneliu Nistor, G. S. D. Beach, and J. L. Erskine*

Department of Physics, The University of Texas at Austin, Austin, Texas, Texas 78712-0264, USA

(Received 31 July 2007; revised manuscript received 20 November 2007; published 11 January 2008)

Oscillations of the field-driven domain-wall (DW) velocity in permalloy nanowires are observed above the Walker breakdown condition using high-speed magneto-optic polarimetry. A one-dimensional analytical model and numerical simulations of DW motion and spin dynamics are used to interpret the experimental data. Velocity oscillations are shown to be much more sensitive to properties of the DW guide structure (which also affect DW mobility) than the DW spin precessional frequency, which is a local property of the material. The results demonstrate the feasibility of experimentally probing the complex field-driven DW dynamics in magnetic nanowires, thereby testing the validity of theoretical models and numerical simulations that describe the dynamics.

DOI: [10.1103/PhysRevB.77.014413](https://doi.org/10.1103/PhysRevB.77.014413)

PACS number(s): 75.60.Ch, 75.70.Kw, 75.75.+a

I. INTRODUCTION

Magnetic-field-driven domain-wall (DW) motion in magnetic nanostructures is a topic of considerable interest.¹⁻⁷ Patterned magnetic nanowires offer prospects for a new generation of spintronic devices⁸⁻¹⁰ and also serve as model systems for exploring fundamental issues related to spin distributions and dynamics in DWs driven by magnetic fields or electric currents.^{4,11} The domain structure in a nanowire consists of head-to-head or tail-to-tail magnetic domains separated by a DW having a width of the order of a few hundreds of nanometers. The spin distribution within stationary or moving DWs can manifest relatively simple or complex behavior. The static spin distributions (no applied field or current) are well understood and can generally be determined by numerically solving Brown's equations based on energy minimization. Phase diagrams that describe how static and dynamic DW spin distributions, i.e., transverse walls (TWs) or vortex walls and the phase boundaries separating DW structures of differing topology, are affected by nanowire cross sectional dimensions have been calculated⁷ and tested by experiments.

The dynamics of DWs in nanowires under field-driven conditions are less well understood. While numerical simulations based on the Landau-Lifschitz-Gilbert (LLG) equation offer one approach to exploring the details of DW dynamics in nanowire structures, direct time-resolved experimental observation of these phenomena on relevant time and spatial scales is not feasible. Progress on these issues will require experimentally tested simulation capability. This paper demonstrates a connection between experimentally detected oscillations in the field-driven DW velocity and the models and simulations that describe the oscillations.

II. EXPERIMENT

One important feature of DW dynamics in nanowires has been established: magnetic DWs are robust under the influence of currents ($j < 10^{12}$ A/m²) and fields; they propagate as entities similar to quasiparticles in solids, and their motion can be described in terms of measurable parameters such as velocities and mobilities, which are sensitive to spin distri-

butions and dynamics within the DWs. Figure 1 illustrates this by displaying a recent measurement³ of the average DW velocity $v \equiv dq/dt$ as a function of drive field for a (vortex structure) DW confined to a permalloy nanowire of cross section of 20 nm thick \times 600 nm wide. The one-dimensional (1D) model and numerical simulation results (also shown) are discussed later. The slope of the $v(H)$ curve at a prescribed value of the applied magnetic field H is the DW mobility $\mu(H)$. The results displayed represent the first complete experimental determination of the mobility function for a nanowire-guided DW over a wide range of H .

The field-driven mobility curve exhibits three regions of qualitatively different behaviors. Region I ($H < H_W$, where H_W is the Walker breakdown field) is well understood in terms of Walker's analytical solution.¹² The propagation of a DW is characterized by a stationary spin distribution in

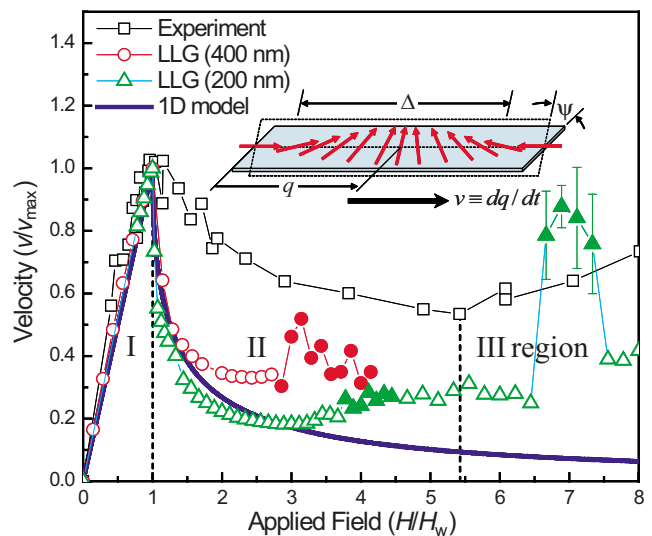


FIG. 1. (Color online) Measured and simulated DW velocity [normalized to $v_{\max} \equiv v(H_W)$] as a function of applied field (normalized to the Walker field H_W). Walker breakdown occurs at $H = H_W$ corresponding to $\psi = \pi/4$. (Inset) Schematic description of the spin distribution within a propagating transverse DW showing tilt angle ψ and wall width Δ . Solid symbols for LLG simulations designate onset of noise in simulated velocity described later in text.

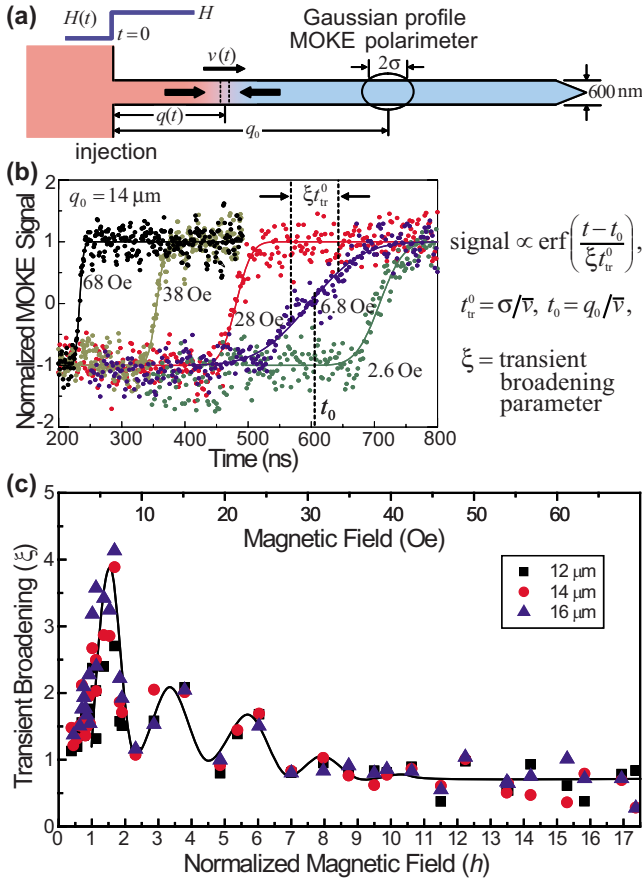


FIG. 2. (Color online) (a) Schematic of DW velocity measurement. (b) Measured transients at different values of H , showing transient broadening effect characterized by the parameter ξ . (c) Plot of $\xi(h)$ for several values of q_0 .

the moving frame that moves at a uniform velocity in a constant applied magnetic field: $v = \mu H$ with mobility $\mu = \gamma \Delta / \alpha$ where γ is the electron gyromagnetic ratio ($\gamma = 1.76 \times 10^7 \text{ Oe}^{-1} \text{ s}^{-1}$), Δ is the DW width, and α is the spin damping constant. The spin configuration within a DW corresponding to region I can be most easily visualized in terms of a TW propagating in a nanowire. In the moving frame of the DW, the stationary spin configuration is described by a canting angle ψ that characterizes the out-of-plane vector direction of spins within the DW (inset in Fig. 1).

The second and third regions of the mobility curve occur above H_W , where the stationary value of ψ is replaced by precessional motion $d\psi/dt \neq 0$. The second region is characterized by a nonlinear negative differential mobility ($dv/dH < 0$) and the third region by a positive linear mobility, similar to what is observed in region I but with a significantly lower value.

The mobility curve (Fig. 1) was determined by magneto-optic Kerr effect (MOKE) polarimetry using a time-of-flight (TOF) technique described in prior publications^{3,14} and outlined in Fig. 2(a). A DW is injected into the nanowire at $t = 0$ by a magnetic field step of amplitude H . The flight time t_0 required for the DW to travel the distance q_0 to the MOKE polarimeter probe spot location yields its average velocity

$\bar{v} = q_0 / t_0$. The velocity can also be determined at the position q_0 by measuring the time $2t_{tr}$ required for the DW to traverse the Gaussian-profile light spot of width 2σ : $v = \sigma / t_{tr}$. The detected transient is represented by an error function produced by the convolution of the wire magnetization (modeled as a traveling step function centered at the DW location) with the Gaussian profile. Figure 2(b) displays selected transients. When $H < H_W$, one has $\bar{v} = v$ because the DW motion is uniform, but for $H > H_W$, the oscillatory motion produces the transient broadening characterized by the parameter $\xi \equiv t_{tr} / t_{tr}^0$ and plotted as a function of H in Fig. 2(c). The parameter ξ characterizes the ratio between the average DW velocity (determined by multiple TOF measurements) and the instantaneous velocity (detected by multiple transient measurements) at the light spot location.

A recent publication³ reported observation of drive-field-dependent broadening in magnetic transients produced by a nanowire-guided DW sweeping across the area probed by a high-speed MOKE polarimeter (Fig. 2). In Ref. 3, the observed transient broadening [Fig. 2(c)] was attributed to velocity oscillations associated with precessional motion of ψ above H_W , but no detailed analysis was presented. The coherent precessional motion of a DW in a permalloy nanowire was later inferred from temporal oscillations in the anisotropic magnetoresistance¹³ but no direct detection of the velocity oscillations has yet been established. In the following sections, we use analytical and numerical models to demonstrate that the transient broadening in Fig. 2(c) is a direct consequence of the velocity oscillations of DW motion above the Walker breakdown.

III. ONE-DIMENSIONAL MODEL

The propagation dynamics of a DW wall can be mathematically described by a one-dimensional model¹¹ that relates ψ and the wall velocity v to parameters associated with the material. A dimensionless form of the model is given by

$$\frac{d\psi}{d\tau} = h - \sin 2\psi, \quad (1)$$

$$v \equiv \frac{dx}{d\tau} = (1 + \alpha^2)h - \frac{d\psi}{d\tau}, \quad (2)$$

where $h \equiv H / H_W$, $x \equiv \alpha q / \Delta = q \gamma H_W / v_{\max}$, $\tau \equiv 2\pi \alpha \gamma M_s t / (1 + \alpha^2)$, $v_{\max} \equiv v(H_W)$, and $H_W \equiv 2\pi \alpha M_s$, where M_s is the saturation magnetization. In this model, the DW velocity is constant for a fixed value of $H < H_W$, and the tilt angle ψ is driven to a stationary value consistent with the strength of the applied field H . At the Walker breakdown field ($h = 1$), the demagnetizing torque, tilt angle ψ , and velocity v reach their maximum values for the Walker solution. If h is increased above $h = 1$, ψ can no longer remain stationary; ψ advances continually, and the demagnetizing torque changes sign each quarter period of ψ rotation. Note that the resulting velocity oscillations occur at twice the rotation frequency $f = \omega / 2\pi$ given by

TABLE I. Parameters from LLG simulations.

Nanowire width (nm)	Walker field (Oe)	v_{\max} (m/s)
600 (Expt.)	4	75
(1D model) ^a	50	1769
200 (LLG) ^b	9	223
400 (LLG) ^b	7	245
600 (LLG) ^b	6	256

^aCalculated for $\alpha=0.01$ and $\Delta=20$ nm.

^bDamping parameter $\alpha=0.01$; thickness=20 nm.

$$\overline{\omega} = \frac{d\psi}{d\tau} = 2\pi f = \sqrt{h^2 - 1} \quad (h > 1). \quad (3)$$

The rotation of ψ becomes more rapid with increasing h , and while the demagnetizing torque that drives DW motion for $h < 1$ averages to zero, for $h > 1$, a small damping torque term cants the wall spins toward H and continues to drive the DW forward.

The 1D model equations [Eqs. (1) and (2)] can be combined to obtain an equation for DW average velocity:

$$\overline{v} \equiv \frac{dx}{d\tau} = (1 + \alpha^2)h - \frac{d\psi}{d\tau} = (1 + \alpha^2)h - \sqrt{h^2 - 1}. \quad (4)$$

When $h < 1$, ψ is stationary and $dx/d\tau$ is constant. With $h > 1$, the precessional motion of ψ , described by Eq. (3), results in oscillatory motion of the DW velocity.

The DW displacement, $x(\tau, \psi_0)$, can be expressed in terms of the average velocity \overline{v} and its variation $\delta v(\tau)$ driven by precessional motion $d\psi/d\tau$. From Eq. (4),

$$v = \overline{v} + \delta v(\tau) = \overline{v} + \sin(2\omega\tau + 2\psi_0), \quad (5)$$

$$x(\tau, \psi_0) = \overline{v}\tau + \int_0^\tau \delta v(\tau) d\tau = \overline{v}\tau + \frac{1}{\omega} \sin(\omega\tau) \sin(\omega\tau + 2\psi_0), \quad (6)$$

where ψ_0 defines the value of ψ at $\tau=0$.

The mobility curve in the 1D model [Eq. (4)] is plotted together with the measured curve in Fig. 1. On scales of normalized field (H/H_W) and velocity [v/v_{\max} , where $v_{\max} = v(H_W)$], the model curve reproduces the essential features of the experiment. However, the 1D model significantly overestimates both the breakdown field and the maximum velocity, as seen in Table I. These differences are due to differences in the breakdown mechanism: uniform wall-plane precession in the 1D model versus vortex nucleation and transverse motion in the experimental geometry.^{1,7}

IV. NUMERICAL SIMULATIONS

In order to account for the dynamics of a more realistic (vortex) DW structure, numerical simulations were performed to complement the analytical model results. Simulations were performed using the University of Texas version

of the LLG Micromagnetics SimulatorTM.¹⁵ This version is a LINUX code compiled to run on the Dell/Cray (Lonestar) cluster (1024 nodes, 64 bit address) of the Texas Advanced Computing Center (TACC). The enhanced computing power (over a single-node version) is very useful for systematic numerical simulation “experiments.”

Simulations were carried out for 20 nm thick nanowires using parameters appropriate to permalloy ($M_s = 800$ emu/cm³, $\alpha=0.01$, and exchange constant $A=1.05 \times 10^{-6}$ erg/cm), with a cell size of $4 \times 4 \times 20$ nm³ and moving boundary conditions. Because the effective magnetic width of the wire in the experiment may be significantly less than its physical width (600 nm) due to formation of magnetically dead regions by focused ion beam milling,¹⁶ simulations were performed for wires of several widths (600, 400, and 200 nm). The calculated mobility curves for two of these widths are shown in Fig. 1.

The values of H_W and v_{\max} obtained from the simulations (listed in Table I) are in much closer agreement with the experimental results than those of the 1D model. Furthermore, the simulations more accurately characterize the finite slope in region III. Some differences still remain between the simulations and the experimental data, both in the values of the breakdown parameters (H_W and v_{\max}) and the rate of the falloff in v in region II. As the simulations were performed for perfect wires, these differences are not surprising. Vortex-mediated breakdown is localized at the sample edges and it is well known¹ that edge roughness can significantly affect the vortex nucleation and/or annihilation process that determines the behavior in this region.

We note that LLG simulations on a fine scale of reduced field manifested a transformation at a critical field to more complex periodic behavior than shown in Fig. 3 (described below). The onset of this more complex behavior occurred at $h \cong 3$ for 400 nm width and $h \cong 4$ and $h \cong 7$ for 200 nm width. This behavior is responsible for the apparent onset of “noise” in the LLG-calculated mobility curves (Fig. 1).

V. VELOCITY OSCILLATIONS AND TRANSIENT BROADENING

The experimental understanding of DW dynamics can be extended by considering not only the average wall velocity (Fig. 1) but also the precessionally driven oscillations about that average for fields $H > H_W$. Equations (5) and (6) show that above breakdown, the velocity varies periodically with time, leading to an oscillatory trajectory of a DW as it propagates along a wire. When the spatial amplitude of these oscillations is comparable to the size of the Kerr laser spot, it becomes possible to detect them. The detected Kerr signal is proportional to the (normalized) magnetization within the field of view, weighted by the Gaussian profile of the MOKE beam. The time-dependent Kerr signal (transient) produced by a DW sweeping across the MOKE beam is hence a function of the wall trajectory $q(t)$.

Figure 3 provides a graphical representation of the mechanism that produces the transient broadening. LLG simulation results for the DW displacement as a function of time are displayed in Fig. 3(a) for two values of drive field H and for

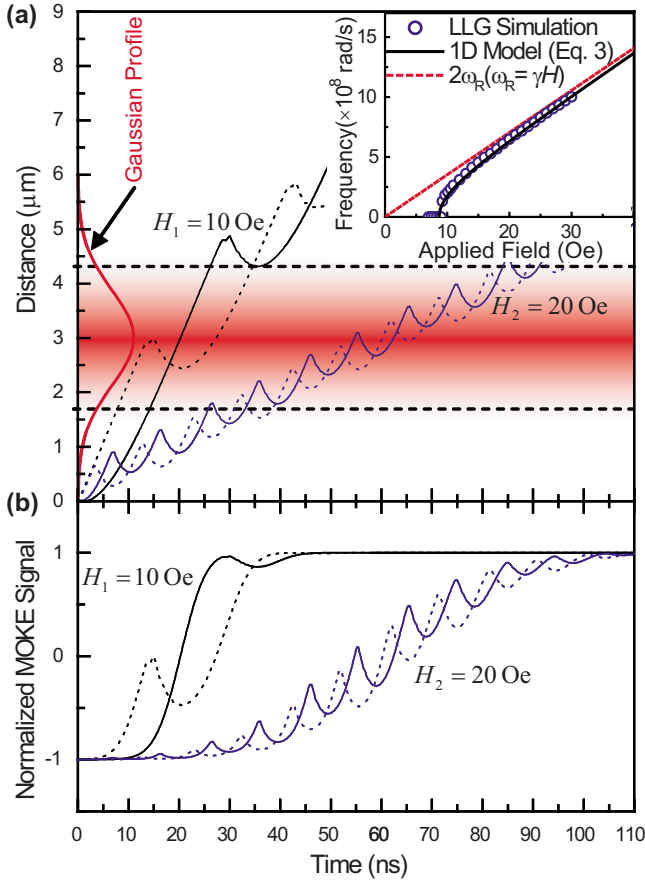


FIG. 3. (Color online) (a) Numerical simulations of DW displacements in a 20 nm thick \times 200 nm wide permalloy nanowire versus time for two values of H above H_w . Gaussian profile centered around $q_0 = 3 \mu\text{m}$ represents MOKE beam. (Inset) DW frequency determined by numerical simulations. (b) Simulated MOKE signal produced by the four displacement records.

two (assumed) values of the initial phase. The average DW velocity $\bar{v}(H)$ for each value of H corresponds to the average slope of $q(t)$, and the oscillations about the average trajectory are apparent in the displacement versus time records. A Gaussian-profile representation of the MOKE beam is plotted centered at $q_0 = 3 \mu\text{m}$ along the displacement axis. The simulated MOKE transients, calculated from $q(t)$ as described below, are displayed in the lower panel for each of the four numerically simulated displacement records.

The transient signal can be simulated by noting that a DW sweeping across the Gaussian MOKE beam located at $x = x_0$ produces a signal proportional to the (normalized) magnetization within the field of view:

$$m(x) = \frac{M(x)}{M_s} = -1 + \frac{2}{\bar{\sigma}\sqrt{\pi}} \int_0^x e^{-((x-x_0)/\bar{\sigma})^2} dx = \text{erf}\left(\frac{x-x_0}{\bar{\sigma}}\right), \quad (7)$$

where $\bar{\sigma} \equiv \alpha\sigma/\Delta$. An analytical expression for the transients in the 1D model can be obtained by inserting $x(t)$ in Eq. (6) into Eq. (7), which yields

$$m(\tau, \psi_0) = \text{erf}\left(\frac{\bar{v}\tau + \frac{1}{\omega} \sin(\omega\tau + 2\psi_0) - x_0}{\bar{\sigma}}\right) = \text{erf}\left(\frac{\tau - \tau_0 + \frac{1}{\bar{v}\omega} \sin(\omega\tau)\sin(\omega\tau + 2\psi_0)}{\tau_{\text{tr}}^0}\right), \quad (8)$$

where dimensionless parameters $\tau_{\text{tr}}^0 = \bar{\sigma}/\bar{v}$ and $\tau_0 = x_0/\bar{v}$ are introduced.

In an actual experiment, 10^4 such transients would be averaged. There are then two limiting cases that must be considered in terms of the initial phase ψ_0 : the coherent limit and the random limit. The former occurs if the initial wall state is precisely repeatable, and the oscillatory propagation occurs in a coherent fashion. The latter case arises if the initial wall phase is random from cycle to cycle or if dephasing occurs as the wall propagates along the wire. The effects resulting from coherent and incoherent signal averagings can be visualized from the simulated transients in Fig. 3(b).

The transient broadening ratio ξ was calculated in each limit using both the 1D model expression for $m(\tau, \psi_0)$ and a series of LLG-simulated displacement records, such as those in Fig. 3(a). The averaged transients were calculated as a function of h in the coherent and random limits as

$$m(\tau, \psi_0 = 0) = \text{erf}\left(\frac{x(\tau, \psi_0 = 0) - x_0}{\bar{\sigma}}\right) \quad (\text{coherent limit}), \quad (9)$$

$$m(\tau) = \frac{1}{N} \sum_{i=0}^N m(\tau, \psi_i = \text{random}) \quad (\text{random limit}), \quad (10)$$

where “random” in Eq. (10) refers to a uniformly distributed random number between 0 and 2π .

Figure 4 displays the results of the analytical simulation of transient broadening based on the 1D model in the coherent and incoherent limits and the corresponding results based on LLG numerical simulations. The results reproduce the essential features of the measured field-dependent broadening in Fig. 2(c). The calculated transient broadening follows an envelope that decreases with increasing field, as does the measured broadening in Fig. 2. This can be understood from the simulated transients in Fig. 3(b). As H increases, the oscillation frequency increases [see Fig. 3(a), inset], and the spatial amplitude decreases. It is apparent from the simulations that the oscillation-induced transient broadening for $H_1 = 10$ Oe will be larger than that produced by the transients at $H_2 = 20$ Oe. The transient broadening also exhibits a series of maxima and minima due to a “beating” effect produced by the velocity oscillations. The condition for maximum broadening may be derived from Eq. (8) and is shown graphically in Fig. 4(b) to correspond to the intersection of the function $2x_0 f(h)/n$ with the (calculated) mobility curve. The function incorporates the normalized displacement x_0 , effective frequency of DW oscillations $2f(h)$, and an integer n . The maximum broadening occurs when $x_0 = n\lambda$ where λ is the effective “wavelength” of a moving DW with frequency of

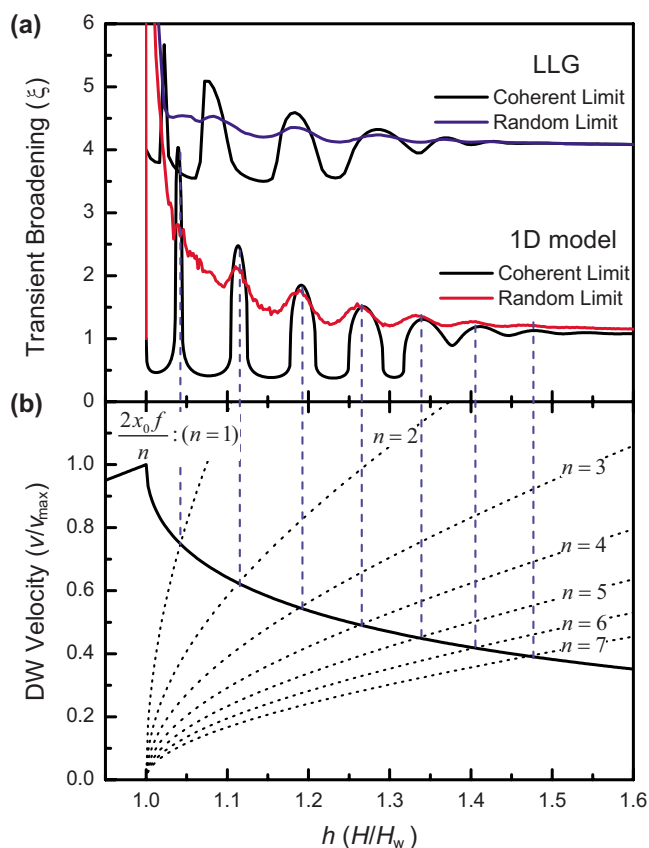


FIG. 4. (Color online) (a) Transient broadening parameters versus reduced field obtained from 1D model and LLG simulations (for 200 nm width) in coherent and incoherent limits. In the simulations, $2\sigma=2\ \mu\text{m}$ and $q_0=8.5\ \mu\text{m}$ were used. The LLG results are vertically offset for clarity. (b) Intersection of the function of the $2x_0f/n$ with the mobility curve (normalized parameters) showing condition for maximum broadening.

$2f$, $\lambda=\bar{v}/2f$. The inability of the 1D model (as well as the numerical simulations) to accurately reproduce the measured mobility curve (compare experiment and simulation curves, Fig. 1) accounts for the large discrepancy between calculated and measured positions of the maxima and minima in the transient broadening as a function of h [compare Figs. 2(c) and 4], but the qualitative features of the 1D model results are consistent with the measured transient broadening.

VI. CONCLUSIONS

Both the 1D model and the numerical simulations (Fig. 4) account for the general features of the transient broadening observed in the experiment in terms of DW velocity oscillations. The damping of oscillations as a function of increasing h results from the higher frequency, smaller spatial amplitude oscillations being averaged by the finite temporal and spatial resolution of the MOKE polarimeter ($2\ \mu\text{m}$, 1 ns). The 1D model and LLG simulations yield very similar $\xi(h)$ behavior, which is unsurprising since both yield very similar (scaled) mobility curves over the range of reduced field where uniform oscillations are produced by the simulation. The inability of the LLG or 1D model to quantitatively reproduce the measured transient broadening [Fig. 2(c)] can be understood based on the sensitivity of the beating condition to the mobility curve [Fig. 4(b)] and the large discrepancy between the measured mobility curve and the 1D model and LLG simulation results (Fig. 1). The excellent agreement between the precessional frequency obtained from the 1D model and the results obtained from the LLG simulation [Fig. 3(a), inset] and the less favorable agreement for $\xi(h)$ [Figs. 3(a) and 2(b)] show that the DW velocity is much more model sensitive than the (local) precessional motion. Note that ω depends on M_s and α , the (local) spin damping parameter, but LLG simulations¹ have shown that the mobility μ depends on (for example) nonlocal edge roughness effects. These results demonstrate a direct connection between a measurable parameter, $\xi(h)$, and the complex oscillatory velocity of a driven DW and provide a sensitive test of models of this behavior. Recent experiments and LLG modeling of the injection process¹⁷ suggest that it may be feasible to approach the coherent limit in experiments. This will improve the diagnostic capability of the technique.

ACKNOWLEDGMENTS

This work was supported by the NSF NIRT program (DMR-0404252) and the R. A. Welch Foundation (F-1015). Instrumentation was developed with support from the NSF IMR program (DMR-0216726) and the Texas Coordinating Board (ATP-0099). Samples were fabricated using facilities of the Center for Nano and Molecular Science and Technology at UT Austin. Simulations were carried out using HPC resources of TACC at UT Austin.

*erskine@physics.utexas.edu

¹Y. Nakatani, A. Thiaville, and J. Miltat, Nat. Mater. **2**, 521 (2003).

²D. Atkinson, D. A. Allwood, G. Xiong, M. D. Cooke, C. C. Faulkner, and R. P. Cowburn, Nat. Mater. **2**, 85 (2003).

³G. S. D. Beach, C. Nistor, C. Knutson, M. Tsoi, and J. L. Erskine, Nat. Mater. **4**, 741 (2005).

⁴G. S. D. Beach, C. Knutson, C. Nistor, M. Tsoi, and J. L. Erskine, Phys. Rev. Lett. **97**, 057203 (2006).

⁵M. Hayashi, L. Thomas, Ya. B. Bazaliy, C. Rettner, R. Moriya, X.

Jiang, and S. S. P. Parkin, Phys. Rev. Lett. **96**, 197207 (2006).

⁶L. Thomas, M. Hayashi, X. Jiang, R. Moriya, C. Rettner, and S. S. P. Parkin, Nature (London) **443**, 197 (2006).

⁷Y. Nakatani, A. Thiaville, and J. Miltat, J. Magn. Magn. Mater. **290**, 750 (2005).

⁸G. A. Prinz, Science **282**, 1660 (1998).

⁹S. A. Wolf, D. D. Awschalom, R. A. Buhrman, J. M. Daughton, S. von Molnár, M. L. Roukes, A. Y. Chtchelkanova, and D. M. Treger, Science **294**, 1488 (2001).

¹⁰D. A. Allwood, G. Xiong, C. C. Faulkner, D. Atkinson, D. Petit,

- and R. P. Cowburn, *Science* **309**, 1688 (2005).
- ¹¹A. Thiaville, Y. Nakatani, J. Miltat, and Y. Suzuki, *Europhys. Lett.* **69**, 990 (2005).
- ¹²A. Hubert and R. Schäfer, *Magnetic Domains* (Springer, Berlin, 1998).
- ¹³M. Hayashi, L. Thomas, C. Rettner, R. Moriya, and S. S. P. Parkin, *Nat. Phys.* **3**, 21 (2007).
- ¹⁴C. Nistor, G. S. D. Beach, and J. L. Erskine, *Rev. Sci. Instrum.* **77**, 103901 (2006).
- ¹⁵M. R. Scheinfein, LLG Micromagnetic Simulator™, <http://llgmicro.home.mindspring.com>
- ¹⁶G. S. D. Beach, C. Knutson, M. Tsoi, and J. L. Erskine (unpublished). Evidence for focused ion beam produced magnetic dead regions at the nanowire edges is based on high-spatial-resolution scans across the nanowire cross section based on MOKE polarimetry.
- ¹⁷G. S. D. Beach, C. Knutson, M. Tsoi, and J. L. Erskine (unpublished).